

Article

Effects of Surface Softening on the Mechanical Properties of an AISI 316L Stainless Steel under Cyclic Loading

Tiehui Fang ^{1,*} and Feng Cai ²¹ College of Mechanics and Electronic Engineering, Wenzhou University, Wenzhou 325035, China² College of Materials Science and Engineering, Hunan University, Changsha 410082, China; fengcai_hnu@163.com

* Correspondence: thfang@wzu.edu.cn; Tel.: +86-137-5507-8105

Abstract: The effects of surface softening on fatigue behavior of AISI 316L stainless steel were investigated. Using cold-rolling and electromagnetic induction heating treatment, a gradient structure was fabricated on AISI 316L stainless steel within which the grain size decreased exponentially from micrometers to nanometers to mimic the surface softening. Stress-controlled fatigue tests were applied to both the gradient and homogeneous structures. Compared with the homogeneous sample, surface softening had no evident effect on fatigue behavior when the stress amplitude was greater than 400 MPa, but significantly deteriorated the fatigue behavior at stress amplitude ≤ 400 MPa. At high-stress amplitude, fatigue behavior is dominated by crack propagation. When the stress amplitude is lowered, strength reduction and stress concentration caused by surface softening accelerate crack initiation and propagation, resulting in an inferior fatigue behavior.

Keywords: surface softening; fatigue; crack initiation; AISI 316L stainless steel; cyclic deformation



Citation: Fang, T.; Cai, F. Effects of Surface Softening on the Mechanical Properties of an AISI 316L Stainless Steel under Cyclic Loading. *Metals* **2021**, *11*, 1788. <https://doi.org/10.3390/met11111788>

Academic Editors: Delphine Retrait and Zhidan Sun

Received: 15 September 2021

Accepted: 4 November 2021

Published: 6 November 2021

Publisher's Note: MDPI stays neutral with regard to jurisdictional claims in published maps and institutional affiliations.



Copyright: © 2021 by the authors. Licensee MDPI, Basel, Switzerland. This article is an open access article distributed under the terms and conditions of the Creative Commons Attribution (CC BY) license (<https://creativecommons.org/licenses/by/4.0/>).

1. Introduction

In most cases, fatigue crack initiates at the surfaces of materials and propagate into the interior [1,2]. Optimization of the surface structure and properties may effectively enhance the global behavior of a material and its service lifetime [3–5]. Surface strengthening technology such as shot peening [6–8], surface mechanical attrition treatment [1,9–11], surface mechanical rolling treatment [2,12,13], and surface mechanical grinding treatment [14–16] can effectively improve the fatigue strength of materials, which have been confirmed by numerous studies. The strength of the surface layer, surface residual compressive stress, and work-hardened surface region play a significant role in enhancing the fatigue limit [17].

However, surface strength is inevitably influenced by working conditions during service. Thermal, chemical, and stress effects are likely to cause surface softening. For example, recrystallization could be triggered by temperature rise induced by friction and wear, which results in surface softening [18]. Grain coarsening is also common in nanograined metals under tension [15], compression [19], or cyclic loading [14,20–22]. In addition, chemical change such as decarburization could induce a surface strength decline of approximately 39% in steel [23,24], resulting in a reduced rolling contact fatigue strength and fretting fatigue strength. Considerable research has been conducted on surface strengthening, but seldom on surface softening. It is believed that surface softening is deleterious to the global fatigue property but its effects and mechanism are unclear. In the present work, by using cold-rolling and subsequent ultra-high-frequency electromagnetic induction heating (EMIH) treatment [25], an inverse gradient nanograined structure (IGNS) layer was fabricated on austenitic 316L stainless steel (SS) to imitate the surface softening. In the IGNS, grain sizes are decreased from micrometers to nanometers with depth. Stress-controlled fatigue testing was applied on both IGNS and homogeneous samples to investigate the effect of surface softening on the fatigue property. The IGNS

sample exhibits different fatigue behavior at different stress amplitudes and the underlying mechanisms are discussed in detail.

2. Materials and Methods

A commercial AISI 316L SS slab (20 mm in thickness) with chemical composition (wt.%): 0.02C, 0.05Si, 1.19Mn, 17.14Cr, 10.16Ni, 2.01Mo, 0.347Cu, 0.146Co, and Fe (balance) was first annealed at 1100 °C for 1 h, and then cold-rolled (CR) to an area reduction of 80% (equivalent true strain to 1.6). Then, EMIH was adopted to fabricate the surface softening sample. In brief, the CR sample was placed at an alternating magnetic field. An induced current was generated in the sample and eventually transformed into heat. Due to the “skin effect”, the induced current tends to concentrate onto the surface and decays exponentially with depth. Consequently, materials at different depths experience recrystallization and grain growth to different extents. Thus, an IGNS surface layer is fabricated on austenitic 316L SS. In this work, an E-05 ultra-high frequency induction heater (Northstar Electronics Co. Ltd. Wenzhou, China, with a maximum frequency ~860 kHz) was used for the EMIH treatment. The duration time was set at 1.3 s and the input power was fixed at 5 kW. During the EMIH treatment, the sample was fixed on a rotator with a rotation speed of 2000 r/min to guarantee uniformity. Meanwhile, the homogeneous sample was obtained through elaborate annealing of the CR sample at 650 °C for 30 min in a T-1200N muffle furnace (hereafter referred to as CRA sample).

Symmetrical stress-controlled push–pull fatigue tests were performed on an MTS-Landmark-100KN electro-hydraulic machine. Fatigue tests were carried out with the stress ratio $R = -1$, sinusoidal wave, and a frequency of 25 Hz. Fatigue specimens were cut into a dog-bone shape with a gauge section of $4 \times 4 \text{ mm}^2$ and a gauge length of 10 mm using a spark wire cutting machine (Figure 1). The load step and number of specimens per test are summarized in Table 1. Prior to fatigue testing, the specimens were ground with SiC grit paper from #400 to #5000 and then electro-polished to obtain a similar surface quality.

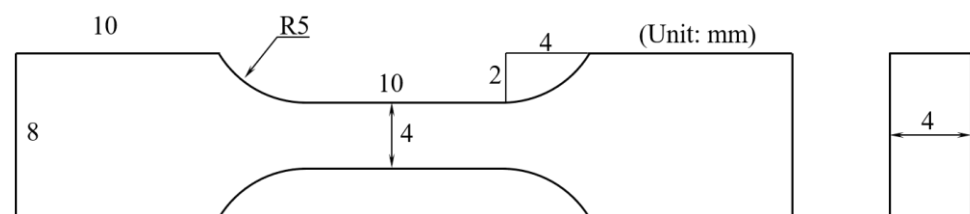


Figure 1. Illustration of the specimen geometry and dimensions.

Table 1. Load step and number of specimens per test.

Sample	Load	750(MPa)	700	650	600	550	500	400	300	250	200	180
	IGNS		1	2	1	1	1	4	4	1		
CRA			2		2		2	2				
CG									1	1	3	2

The cross-sectional morphology of the IGNS sample was characterized by using a scanning electronic microscope (SEM) with an attachment of electron backscattered diffraction (EBSD). The fracture surface was examined by SEM with secondary electron mode. Detailed microstructural characterizations of the IGNS surface layer were performed on a JEOL–3010 high-resolution transmission electron microscopy (HR-TEM) operating at a voltage of 200 kV.

The hardness variation was measured on a microhardness tester with a load of 200 g and a holding time of 10 s. Uniaxial tensile tests were performed on an Instron 5982 system with a strain rate of $5 \times 10^{-3} \text{ s}^{-1}$ at ambient temperature. The residual stress values were

measured by Proto–IXRD. A Rigaku MiniFlex X-ray diffractometer (XRD) with Cu K α radiation was used to determine the phase constitutions. The scan angle ranged from 40° to 140° with a step size of 0.02°.

3. Results

3.1. Microstructure Characterization of IGNS and CRA Sample

Figure 2a shows the typical cross-sectional microstructure of the IGNS sample. Clear evidence of recrystallization was observed on the surface. With increasing depth, both the volume fraction and grain size of recrystallization are decreased as the thermal effect decays. When the depth exceeded 250 μm , the deformed structure remains intact, and plastic deformation streamlines are well preserved. Detailed microstructure was revealed by SEM and HR-TEM. At the top-most surface, the deformed structure was entirely recrystallized as revealed by electron backscatter diffraction (EBSD), as shown in Figure 2b. Recrystallized grains were equiaxed, with an average grain size of $3 \pm 1.6 \mu\text{m}$. At a depth of 100 μm (Figure 2c), recrystallization consumes most nanograins in shear bands. Statistical TEM measurements indicate that the average grain size reached $278 \pm 89 \text{ nm}$ in this layer. With the depth increased to 250 μm (Figure 2d), recrystallization was rarely detected. Instead, recovery occurred in nanograins and nanotwins. When the depth exceeded 250 μm , deformed structures remained unchanged except for an evident decline in the dislocation density. According to the observation, an IGNS layer was successfully fabricated to simulate the surface softening.

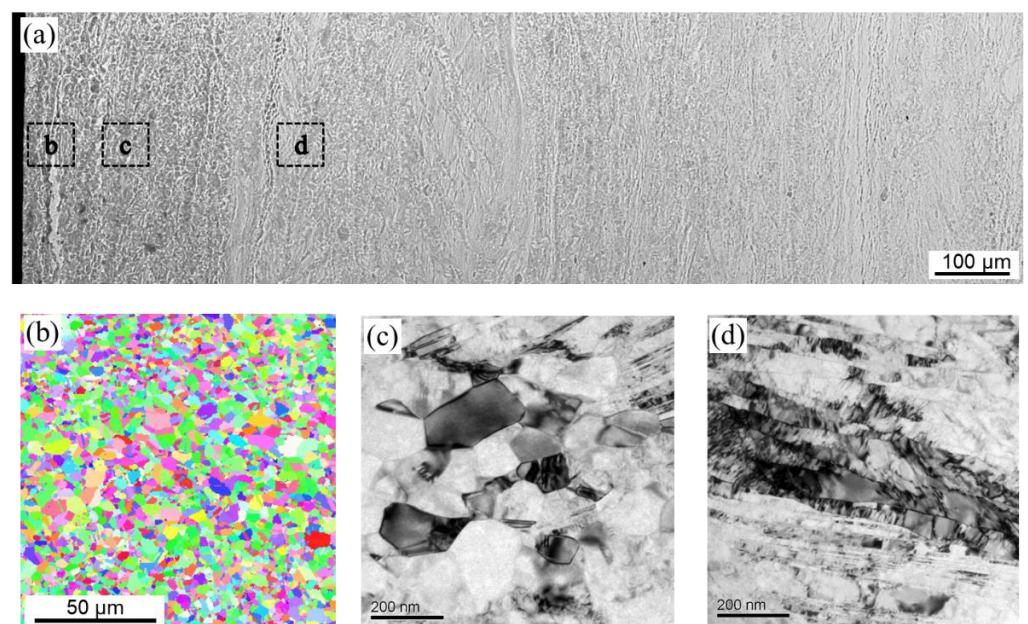


Figure 2. Typical microstructure of the inverse gradient nanostructure. (a) Overall picture. (b) EBSD image of the top-most surface. TEM image at depth of (c) 100 μm and (d) 250 μm .

The homogeneous sample was obtained through elaborate annealing of the CR sample. After annealing, the microstructure of the CRA sample was similar to the core structure of the IGNS sample, as shown in Figure 3a. Plastic deformation streamlines were evident. TEM observation (Figure 3b) confirmed that recovery prevails in the CRA sample and recrystallization was absent. Grain size remained the same as the initial CR structure.

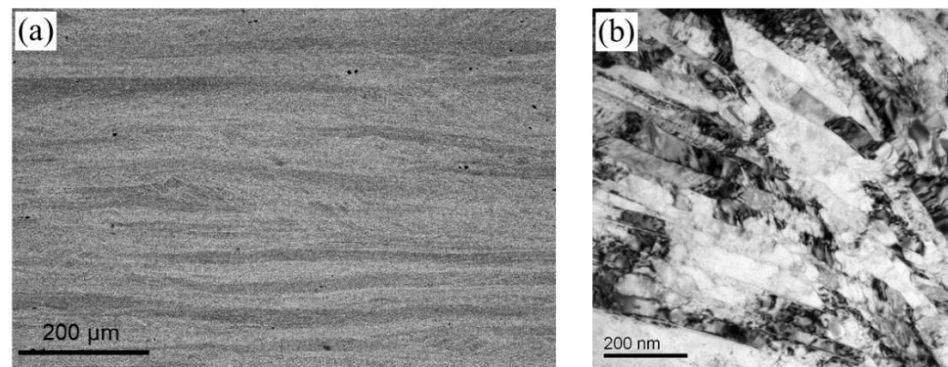


Figure 3. (a) ECC image of the uniform structure (as-cold rolled). (b) TEM bright field image of the cold rolled sample annealed at 650 °C for 30 min.

Figure 4 shows the XRD profile of different samples. The coarse-grained (CG) sample was completely composed of austenite phase (γ) and no peak of the martensite phase (α) could be observed. Deformation-induced martensite phase was absent after CR treatment due to temperature rise during deformation [26]. For the IGNS and CRA sample, diffraction peaks indicate that all of them were single-phase austenite. No new phase appeared. The change in the relative intensity of the diffraction peaks was due to the difference in the view plane. Phase analysis eliminated the interference of martensite (or other secondary phases) on the fatigue properties.

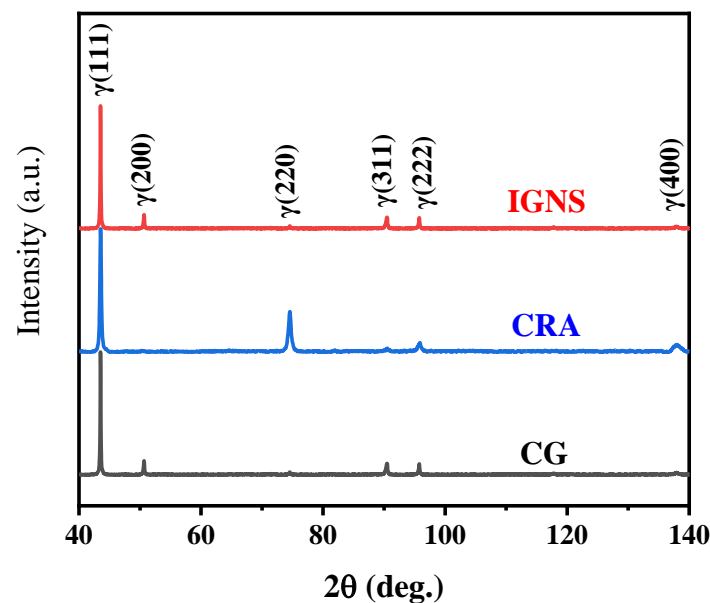


Figure 4. XRD profiles of the samples in various conditions.

3.2. Mechanical Properties of IGNS and CRA Sample

Figure 5a presents the cross-sectional hardness profile in different conditions. Results showed that the CRA sample achieved a high hardness of 4.18 ± 0.09 GPa, slightly lower than the CR sample (4.44 ± 0.01 GPa). The fluctuation was relatively small, indicating a homogeneous structure in the CRA sample. In contrast, a gradient distribution of hardness was present in the IGNS sample. The hardness initiated from 2.44 GPa at the topmost surface and increased gradually with depth. At a depth of 250 μm , it leveled off at about 4.18 GPa, which is close to the hardness of the CRA sample. Beyond the depth of 250 μm , the hardness of the IGNS sample overlapped that of the CRA sample and denotes that the only difference between IGNS and CRA samples is the softened surface layer. For

comparison, the CG sample possessed the lowest hardness of 1.31 ± 0.05 GPa. From the hardness results, the thickness of the IGNS layer was estimated to be $250 \mu\text{m}$, which is consistent with the TEM observation.

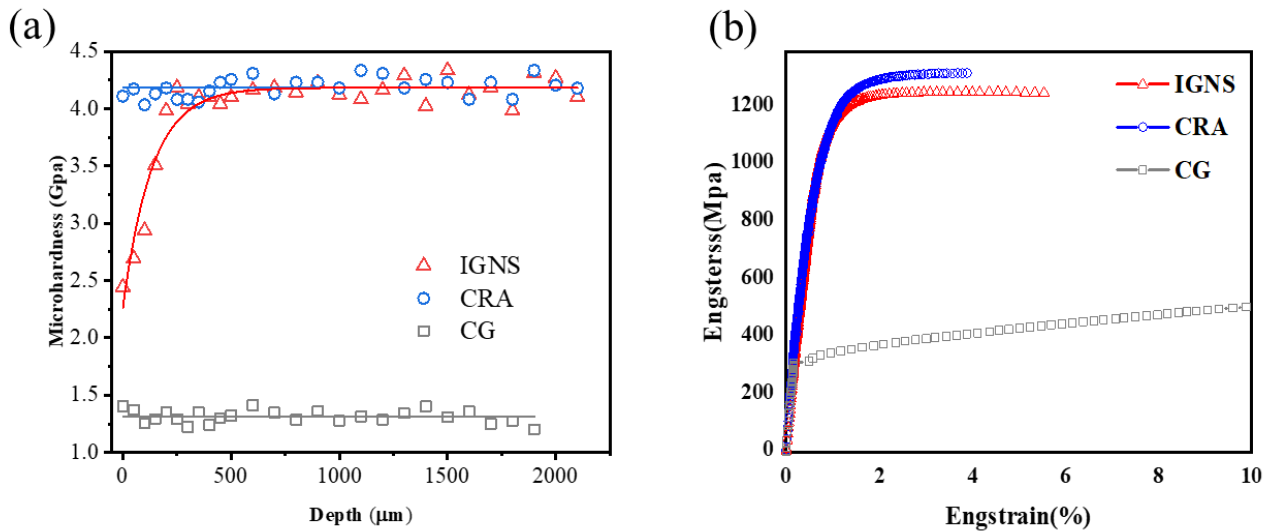


Figure 5. (a) Cross-sectional hardness profiles and (b) uniaxial tensile curves of samples in various conditions.

Corresponding uniaxial tensile tests are displayed in Figure 5b. The CG sample yielded at 305 MPa and obtained a uniform elongation of 40%. For the IGNS and CRA samples, the yield strength ($\sigma_{0.2\%}$) and uniform elongation were 1113 ± 35 MPa, $5.9 \pm 1.2\%$, and 1144 ± 26 MPa, $3.8 \pm 0.3\%$, respectively. The yield strength of the IGNS sample was only ~ 30 MPa lower than that of the CRA sample due to surface softening. However, the uniform elongation was evidently improved. TEM, hardness, and tensile results confirmed that the only difference between the IGNS and CRA sample was the softened surface.

3.3. Fatigue Behavior of the IGNS and CRA Sample

The Wöhler stress amplitude–number of cycles (S–N) curves of the IGNS, CG, and CRA samples are shown in Figure 6. Compared with the CG sample, the CRA sample exhibited significant improvement in both the fatigue life and the fatigue strength. For instance, the CRA sample maintained a cycle life of 2.3×10^4 at the stress amplitude of 700 MPa, while it was 250 MPa for the CG sample at a similar cycle life (1.4×10^4). At a cyclic life of 6.4×10^5 , the fatigue strength of the CRA sample was elevated to ~ 400 MPa, over 100% higher than that of the CG sample. In contrast, the fatigue behavior of the IGNS sample was distinctly different. When the stress amplitude was high, the fatigue life of the IGNS sample was similar to the CRA sample. This trend persisted to the stress amplitude of 500 MPa. Surface softening caused no significant impact on fatigue behavior. As the stress amplitude decreased to 400 MPa, the cyclic life of the IGNS sample (only $\sim 1.4 \times 10^5$) was greatly reduced relative to the CRA sample ($\sim 6.4 \times 10^5$). When the stress amplitude further decreased, the cyclic life of the IGNS sample followed the current trend.

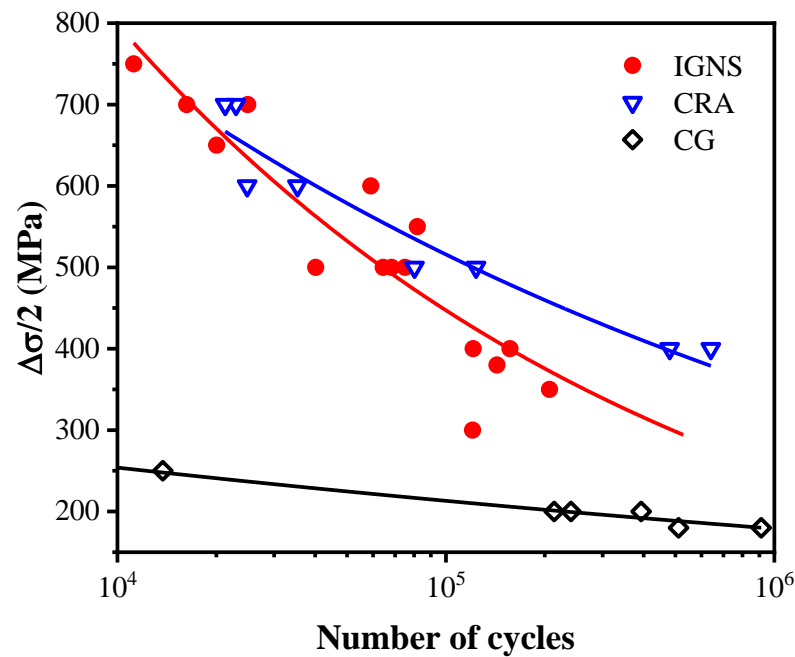


Figure 6. S–N curves of samples in various conditions. The fitted lines follow the Basquin equation.

3.4. Fractography

Because the fatigue behaviors of the IGNS and CRA samples changed at a stress amplitude of 400 MPa, the fractography was focused on 500 MPa (Figure 7) and 400 MPa (Figure 8). At the stress amplitude of 500 MPa, the cycle number of the two samples were close. Similar fractography was obtained in both samples, as can be seen from Figure 7a,d. Cracks started on one side of the surface and extended to the other until an instantaneous fracture occurred. Areas of crack initiation and propagation were similar in shape and size. Careful observation (Figure 7b,d) revealed subtle differences between these two samples. The crack initiation region of the CRA sample was tortuous, which is the result of multiple crack initiation and coalescence. In contrast, the edge was relatively flat in the IGNS sample, which means that the crack started from one single source and then expanded rapidly. This difference was especially obvious when the stress amplitude was 400 MPa. As shown in Figure 8a, cracks in the CRA sample started from multiple positions and propagated independently (marked by arrows). In contrast, the fatigue crack in the IGNS sample was still developed from a single initial crack (Figure 8b). The crack initiation area was flat and smooth, indicating that the crack initiation and propagation process was relatively easy. By comparing Figures 7d and 8b, it can be seen that the fracture morphology of the IGNS samples was very similar under different stress amplitudes.

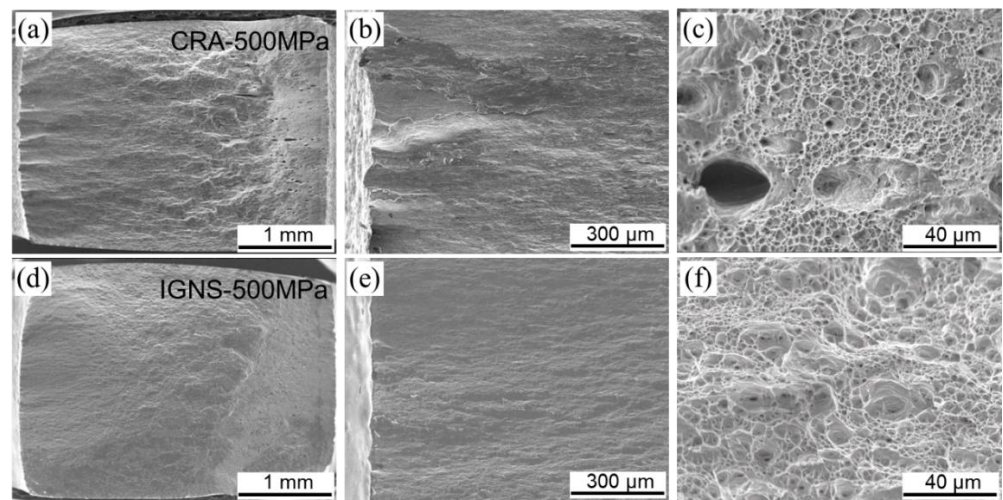


Figure 7. Fractography of (a) the CRA sample and (d) the IGNS sample under stress amplitude of 500 MPa. (b,c) and (e,f) show the crack initiation and final fracture area of the CRA and IGNS sample, respectively.

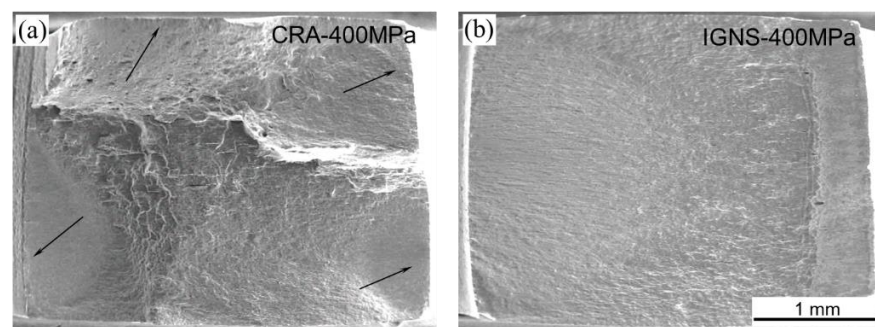


Figure 8. Fractography of (a) the CRA sample and (b) the IGNS sample under a stress amplitude of 400 MPa.

4. Discussion

Compared with the homogeneous structure, the cyclic deformation behavior of the IGNS sample was clearly divided into two stages. When the stress amplitude exceeded 400 MPa, the performance of the IGNS sample was not different from that of the CRA sample. When the stress amplitude was less than 400 MPa, the fatigue life of the IGNS sample was significantly lowered. In this section, the effects of surface softening on the fatigue behavior were analyzed in various stress amplitudes, in terms of crack initiation and propagation, cyclic deformation behaviors, and residual stress.

4.1. Effect of Surface Softening on Fatigue Behavior at Stress Amplitude >400 MPa

The S–N curve shows that the surface softening had no obvious effect on the fatigue life when the stress amplitude was larger than 400 MPa, relative to the CRA sample. There are three reasons for this phenomenon. First, when the stress amplitude is greater than >400 MPa, both samples are in the low-cycle fatigue zone and the proportion of crack initiation to the whole fatigue life is low. Crack initiation was relatively easy in both samples. Therefore, the difference in crack initiation rate had little effect on the overall life, although surface softening did accelerate crack initiation. Second, the gradient structure (especially with inverse grain size distribution) is beneficial to hinder crack propagation. As shown in Figure 7, the crack propagation area of the IGNS sample was larger than that of the CRA sample, which means that more energy is expended on crack propagation in the IGNS sample. Recrystallized grains along the crack growth path consume energy and

blunt the crack tip (Figure 2c). Kermanidis [27] et al. found that the crack growth rate in the negative gradient structure (i.e., the grain size gradually decreases) was lower than that in the uniform and positive gradient aluminum alloys. Third, the coarse grains on the surface impart a strong work hardening ability to the IGNS sample. The cross-section hardness of the IGNS sample changed significantly before and after fatigue, as shown in Figure 9. The hardness of the surface layer was greatly increased from 2.44 GPa to 4.155 GPa. Meanwhile, the hardness outside the IGNS layer remained unchanged. The results showed that the surface softening layer underwent significant work hardening during fatigue, and work hardening helped to restrain the growth of fatigue cracks.

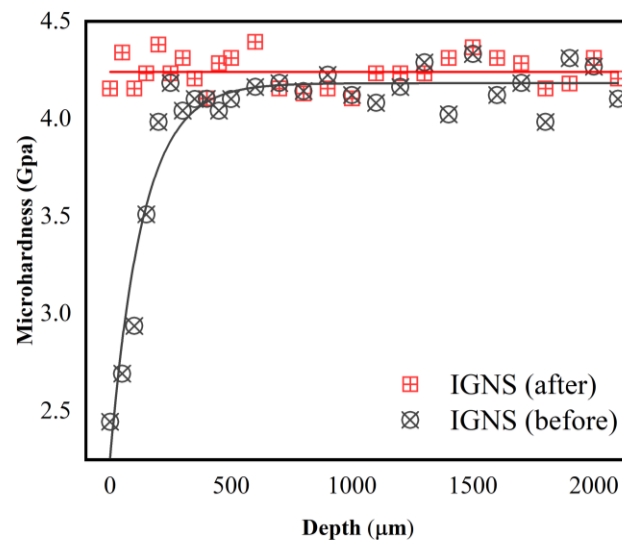


Figure 9. Cross-sectional hardness profiles of the IGNS sample before and after fatigue at a stress amplitude of 700 MPa.

4.2. Effect of Surface Softening on Fatigue Behavior at Stress Amplitude ≤ 400 MPa

When the stress amplitude was lower than 400 MPa, the fatigue life of the IGNS sample was significantly lower than that of the CRA sample. Under this stress range, the material enters the high-cycle fatigue region. A significant feature of high-cycle fatigue is that the proportion of the crack initiation stage to the total fatigue life increases significantly. Experiments carried out on the AlSi7Mg06 alloy proved that the portion of crack initiation increased with the increase in total fatigue life [28]. In the 316L samples treated by surface mechanical rolling at low-stress amplitude, the crack initiation stage even exceeded 90% [2]. Figure 10 shows the cyclic deformation strain curves of the IGNS and CRA samples under different stress amplitudes. For higher stress amplitude, the behavior was significantly different. After the initial stage, there was a visible reduction in the strain amplitude for the IGNS 700 MPa sample. The reduced strain amplitude indicates cyclic hardening, which is attributed to the work hardening of the IGNS layer. However, for the CRA sample, it was almost constant. For the stress amplitude of 400 MPa, the same behavior of CRA and IGNS was rather visible.

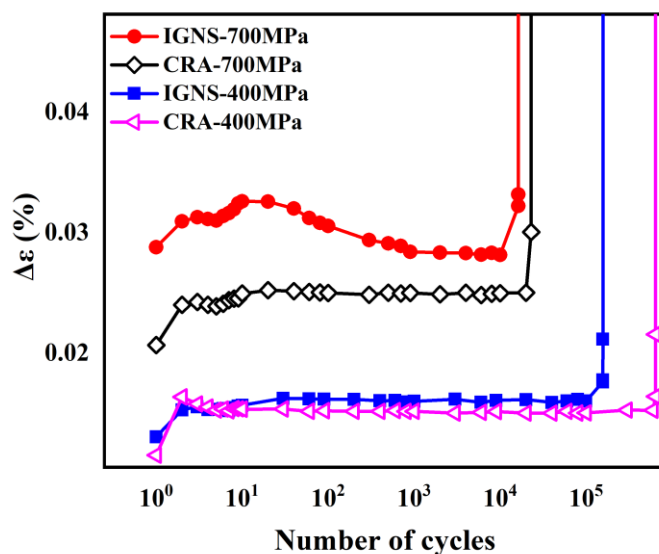


Figure 10. Cyclic deformation curves of the IGNS and CRA samples under different stress amplitudes.

Recrystallization significantly reduces the yield strength of the surface. Based on the statistics, the surface yield strength can be calculated as 335 MPa (according to the Hall–Petch relationship [29]). Grains on the IGNS sample surface yielded under the stress amplitude, resulting in permanent deformation and premature crack initiation. In contrast, the CRA sample was elastic under the same stress amplitude and the crack initiation stage was substantially prolonged. It can also be seen from the cyclic strain curve (Figure 10) that the strain amplitude of the IGNS sample in a steady state was larger than the CRA sample. The extra strain amplitude came from the permanent deformation of the surface. Due to the large proportion of crack initiation in the high cycle fatigue, the divergence in the crack initiation stage between the IGNS and CRA samples resulted in a significant difference in the total fatigue life.

4.3. Effects of Surface Softening on Fatigue Behavior

According to the above analysis, the influence of surface softening on the fatigue behavior is mainly to reduce the threshold of crack initiation and shorten the crack initiation stage. Figure 11 clearly shows this difference. Before cyclic deformation, the surface quality was the same in the IGNS (Figure 11a) and CRA samples (Figure 11c). When the cyclic number reached 1.0×10^4 , slip traces appeared on the IGNS sample surface (Figure 11b). These traces developed into large intrusions and extrusions in the subsequent deformation process and became the source of crack initiation. With an even higher cyclic number (1.3×10^4), the surface morphology of the CRA sample remained the same as the initial state (Figure 11d). This result is consistent with previous literature where the crack initiation tendency decreases with grain refinement [30].

On the other hand, coarse recrystallized grains affect the crack growth rate in the primary stage. It is generally recognized that a structure with a relatively larger grain size tends to have a higher fatigue-crack-growth threshold and lower crack-growth rate [31–34]. CG steel exhibited an enhanced fatigue crack growth resistance due to the more tortuous fatigue crack path and roughness-induced crack closure effect, compared to the nano-grained counterpart [32]. Cao RQ et al. specifically measured crack growth rates in gradient and uniform structures [35]. It was found that both normal and inverse gradient structures displayed a much-improved toughness compared to uniform grain-sized materials. Particularly, the inverse gradient (i.e., CG→NG) specimen was far superior to the normal gradient structure in the crack-initiation toughness, which is ascribed to excessive crack-tip blunting in the coarse-grained microstructure. Therefore, it can be inferred that the coarse

grains formed by surface softening can effectively absorb the energy of crack growth and reduce the crack growth rate.

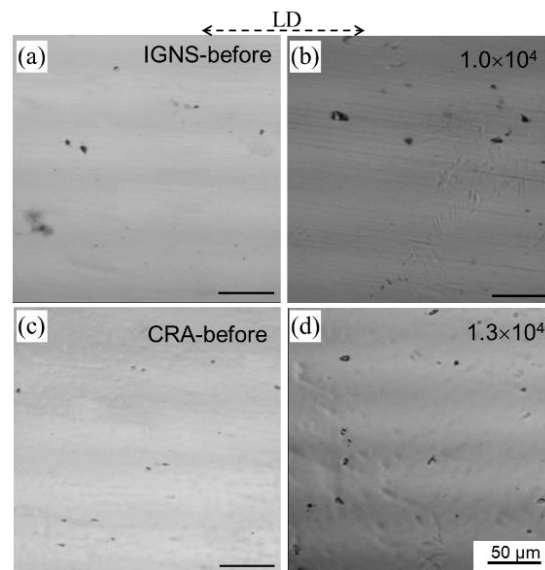


Figure 11. Surface morphology of the IGNS sample (a) before and (b) after cyclic deformed to 1.0×10^4 , compared with the CRA sample (c) before and (d) after cyclic deformed to 1.3×10^4 at a stress amplitude of 700 MPa.

Surface softening directly affects the fatigue strength of the material. Empirically, the stress-controlled fatigue behavior of a material is typically described by the Basquin equation as [36]:

$$\sigma_a = \sigma'_f (2N_f)^b \quad (1)$$

where N_f is the number of cycles to failure; σ_a is stress amplitude; b is the fatigue strength exponent; and σ'_f is the fatigue strength coefficient. According to Equation (1), σ'_f and b were determined and listed in Table 2. Statistics show that the fatigue strength exponent b of the CRA sample was ~ 0.16 (in absolute value), consistent with the reported data [37,38]. In comparison, it was found that b was extraordinarily high in the IGNS samples. The literature [39] demonstrated that b is influenced by strain localization at the crack initiation stage as well as the stress gradient at the crack propagation stage. In the IGNS sample, the softened surface layer imparts a lower resistance to fatigue crack initiation and strain localization. Therefore, b is expected to be increased during both the crack initiation and propagation stages. As the proportion of crack initiation in the total fatigue life increases, the performance of materials in high cycle fatigue depends largely on the crack initiation. Surface softening significantly reduces the threshold of crack initiation; therefore, the high cycle fatigue performance of the material is largely determined by the surface strength.

Table 2. Mechanical and derived fatigue parameters of CG, IGNS, and CRA samples according to Equation (1) in comparison with those obtained in dynamic plastic deformation (DPD), data from [38] and equal channel angular presson (ECAP), data from [37].

Sample	σ_u (MPa)	σ'_f (MPa)	b
CG	644	539	−0.08
IGNS	1241	9651	−0.25
CRA	1310	3912	−0.16
DPD	1190	1812	−0.10
ECAP	1340	1367	−0.11

4.4. Effects of Residual Stress on Fatigue Behavior

Compressive residual stresses are suggested to improve the fatigue properties by increasing the surface resistance to crack initiation as well as reducing the crack propagation rate [40]. In this work, the residual stress in the surface layer of the CG, CRA, and IGNS samples was measured by XRD, as listed in Table 3. The averaged residual stress of the CG sample was -56 ± 34 MPa. The influence of residual stress was negligible. Compressive residual stresses were induced in the surface layer by CR and most of them were retained after annealing. As shown in Table 3, the residual stresses in the CRA and IGNS samples were -417 ± 43 and -384 ± 18 MPa, respectively. These two values were very close. The fatigue life of the two materials was also similar in the stress range of 400~700 MPa. Therefore, it might be concluded that residual stress is not the main reason for the difference in fatigue properties. Other studies have shown that the main relaxation of residual stress normally takes place in the first few cycles [41,42], and residual stress has little effect on the followed lifetime.

Table 3. Residual stress of the surface layer in the CG, IGNS, and CRA sample.

Sample	Residual Stress (MPa)
CG	-56 ± 34
IGNS	-384 ± 18
CRA	-417 ± 43

5. Conclusions

By using a gradient structure, the effect of surface softening on fatigue performance was studied.

Stress-controlled tension-compression fatigue results show that the surface softening affects crack initiation. When the stress amplitude is high, the proportion of the crack initiation stage to the whole life is relatively low. Therefore, the fatigue life of the gradient sample is close to that of the homogenous sample. When the stress amplitude is lower than a critical value, the fatigue behavior of the gradient sample is deteriorated due to the accelerated crack nucleation. The critical stress amplitude is close to the surface strength.

Author Contributions: Conceptualization, T.F.; Methodology, T.F.; Validation, F.C.; Formal analysis, F.C. and T.F.; Investigation, F.C. and T.F.; data curation, T.F.; Writing—original draft preparation, F.C.; Writing—review and editing, T.F.; Supervision, T.F.; Project administration, T.F.; Funding acquisition, T.F. All authors have read and agreed to the published version of the manuscript.

Funding: This research was funded by the National Nature Science Foundation of China (Grant No. 51701069) and the Fundamental Research Funds for the Central Universities (Grant No. 531107040867).

Institutional Review Board Statement: Not applicable.

Informed Consent Statement: Not applicable.

Data Availability Statement: Not applicable.

Conflicts of Interest: The authors declare no conflict of interest.

References

- Huang, H.W.; Wang, Z.B.; Lu, J.; Lu, K. Fatigue behaviors of AISI 316L stainless steel with a gradient nanostructured surface layer. *Acta Mater.* **2015**, *87*, 150–160. [[CrossRef](#)]
- Sun, Z.; Reiraint, D.; Baudin, T.; Helbert, A.L.; Brisset, F.; Chemkhi, M.; Zhou, J.; Kanouté, P. Experimental study of microstructure changes due to low cycle fatigue of a steel nanocrystallised by Surface Mechanical Attrition Treatment (SMAT). *Mater. Charact.* **2017**, *124*, 117–121. [[CrossRef](#)]
- Lu, K.; Lu, J. Surface nanocrystallization (SNC) of metallic materials—presentation of the concept behind a new approach. *J. Mater. Sci. Technol.* **1999**, *15*, 193–197.

4. Liu, G.; Lu, J.; Lu, K. Surface nanocrystallization of 316L stainless steel induced by ultrasonic shot peening. *Mater. Sci. Eng. A* **2000**, *286*, 91–95. [[CrossRef](#)]
5. Tao, N.R.; Lu, J.; Lu, K. Surface nanocrystallization by surface mechanical attrition treatment. *Mater. Sci. Forum* **2008**, *579*, 91–107. [[CrossRef](#)]
6. Gao, Y.K.; Yao, M.; Zhao, S. Another mechanism for fatigue strength improvement of metallic parts by shot peening. *J. Mater. Eng. Perform.* **2003**, *12*, 507–511. [[CrossRef](#)]
7. Masaki, K.; Ochi, Y.; Matsumura, T. Initiation and propagation behaviour of fatigue cracks in hard-shot peened Type 316L steel in high cycle fatigue. *Fatigue Fract. Eng. Mater. Struct.* **2010**, *27*, 1137–1145. [[CrossRef](#)]
8. Bagherifard, S.; Fernandez-Pariente, I.; Ghelichi, R.; Guagliano, M. Effect of severe shot peening on microstructure and fatigue strength of cast iron. *Int. J. Fatigue* **2014**, *65*, 64–70. [[CrossRef](#)]
9. Sun, Z.; Zhou, J.; Reiraint, D.; Baudin, T.; Helbert, A.-L.; Brisset, F.; Kanouté, P. Low cycle fatigue of 316L stainless steel processed by surface mechanical attrition treatment (SMAT). *MATEC Web Conf.* **2018**, *165*, 15002. [[CrossRef](#)]
10. Zhou, J.; Reiraint, D.; Sun, Z.; Kanouté, P. Comparative study of the effects of surface mechanical attrition treatment and conventional shot peening on low cycle fatigue of a 316L stainless steel. *Surf. Coat. Technol.* **2018**, *349*, 556–566. [[CrossRef](#)]
11. Zhou, J.; Sun, Z.; Kanouté, P.; Reiraint, D. Effect of surface mechanical attrition treatment on low cycle fatigue properties of an austenitic stainless steel. *Int. J. Fatigue* **2017**, *103*, 309–317. [[CrossRef](#)]
12. Zhang, K.; Wang, Z.B.; Lu, K. Enhanced fatigue property by suppressing surface cracking in a gradient nanostructured bearing steel. *Mater. Res. Lett.* **2017**, *5*, 258–266. [[CrossRef](#)]
13. Lei, Y.B.; Wang, Z.B.; Xu, J.L.; Lu, K. Simultaneous enhancement of stress- and strain-controlled fatigue properties in 316L stainless steel with gradient nanostructure. *Acta Mater.* **2019**, *168*, 133–142. [[CrossRef](#)]
14. Yang, L.; Tao, N.R.; Lu, K.; Lu, L. Enhanced fatigue resistance of Cu with a gradient nanograined surface layer. *Scr. Mater.* **2013**, *68*, 801–804. [[CrossRef](#)]
15. Fang, T.H.; Tao, N.R.; Lu, K. Tension-induced softening and hardening in gradient nanograined surface layer in copper. *Scr. Mater.* **2014**, *77*, 17–20. [[CrossRef](#)]
16. Long, J.; Pan, Q.; Tao, N.; Dao, M.; Suresh, S.; Lu, L. Improved fatigue resistance of gradient nanograined Cu. *Acta Mater.* **2018**, *166*, 56–66. [[CrossRef](#)]
17. Dai, K.; Shaw, L. Analysis of fatigue resistance improvements via surface severe plastic deformation. *Int. J. Fatigue* **2008**, *30*, 1398–1408. [[CrossRef](#)]
18. Gao, Q.Y.; Li, S.X.; Su, Y.S.; Cao, J.; Moliar, O. Grain coarsening of nano laminated structure in martensite steel under sliding wear. *Tribol. Int.* **2020**, *151*, 106381. [[CrossRef](#)]
19. Brandstetter, S.; Zhang, K.; Escudro, A.; Weertman, J.R.; Swygenhoven, H.V. Grain coarsening during compression of bulk nanocrystalline nickel and copper. *Scr. Mater.* **2008**, *58*, 61–64. [[CrossRef](#)]
20. Long, J.Z.; Pan, Q.S.; Tao, N.R.; Lu, L. Abnormal grain coarsening in cyclically deformed gradient nanograined Cu. *Scr. Mater.* **2018**, *145*, 99–103. [[CrossRef](#)]
21. Mughrabi, H.; Hppel, H.W. Cyclic deformation and fatigue properties of very fine-grained metals and alloys. *Int. J. Fatigue* **2010**, *32*, 1413–1427. [[CrossRef](#)]
22. Vinogradov, A.; Hashimoto, S. Multiscale Phenomena in Fatigue of Ultra-Fine Grain Materials & mdash; an Overview. *Mater. Trans.* **2001**, *42*, 74–84.
23. Zhao, X.J.; Guo, J.; Wang, H.Y.; Wen, Z.F.; Liu, Q.Y.; Zhao, G.T.; Wang, W. Effects of decarburization on the wear resistance and damage mechanisms of rail steels subject to contact fatigue. *Wear* **2016**, *364–365*, 130–143. [[CrossRef](#)]
24. Waterhouse, R.; Taylor, D. The Effect of Heat Treatment and Decarburization on the Fretting Fatigue Behaviour of a 0.7 per Cent Carbon Steel. *Proc. Instn. Mech. Engrs.* **1970**, *185*, 691–695. [[CrossRef](#)]
25. Long, Q.Y.; Lu, J.X.; Fang, T.H. Microstructure and mechanical properties of AISI 316L steel with an inverse gradient nanostructure fabricated by electro-magnetic induction heating. *Mater. Sci. Eng. A* **2019**, *751*, 42–50. [[CrossRef](#)]
26. Yan, F.K.; Liu, G.Z.; Tao, N.R.; Lu, K. Strength and ductility of 316L austenitic stainless steel strengthened by nano-scale twin bundles. *Acta Mater.* **2012**, *60*, 1059–1071. [[CrossRef](#)]
27. Kermanidis, A.T.; Tzamtzis, A. An experimental approach for estimating the effect of heat affected zone (HAZ) microstructural gradient on fatigue crack growth rate in aluminum alloy FSW. *Mater. Sci. Eng. A* **2017**, *691*, 110–120. [[CrossRef](#)]
28. Wagner, D.; Ranc, N.; Bathias, C.; Paris, P.C. Fatigue crack initiation detection by an infrared thermography method. *Fatigue Fract. Eng. Mater. Struct.* **2009**, *33*, 12–21. [[CrossRef](#)]
29. Kashyap, B.P. Towards interrelationship of grain size, cell parameters and flow stress in type 316L stainless steel. *Acta Mater.* **2002**, *50*, 2413–2427. [[CrossRef](#)]
30. Cavaliere, P. Fatigue properties and crack behavior of ultra-fine and nanocrystalline pure metals. *Int. J. Fatigue* **2009**, *31*, 1476–1489. [[CrossRef](#)]
31. Chowdhury, P.B.; Sehitoglu, H.; Rateick, R.G.; Maier, H.J. Modeling fatigue crack growth resistance of nanocrystalline alloys. *Acta Mater.* **2013**, *61*, 2531–2547. [[CrossRef](#)]
32. Ma, P.; Qian, L.; Meng, J.; Liu, S.; Zhang, F. Fatigue crack growth behavior of a coarse- and a fine-grained high manganese austenitic twin-induced plasticity steel. *Mater. Sci. Eng. A* **2014**, *605*, 160–166. [[CrossRef](#)]

33. Yin, D.; Liu, H.; Chen, Y.; Yi, D.; Bo, W.; Wang, B.; Shen, F.; Fu, S.; Tang, C.; Pan, S. Effect of grain size on fatigue-crack growth in 2524 aluminium alloy. *Int. J. Fatigue* **2016**, *84*, 9–16. [[CrossRef](#)]
34. Turnbull, A.; Rios, E. The effect of grain size on fatigue crack growth in an aluminium magnesium alloy. *Fatigue Fract. Eng. Mater. Struct.* **2010**, *18*, 1355–1366. [[CrossRef](#)]
35. Cao, R.; Yu, Q.; Pan, J.; Lin, Y.; Sweet, A.; Li, Y.; Ritchie, R.O. On the exceptional damage-tolerance of gradient metallic materials. *Mater. Today* **2020**, *32*, 94–107. [[CrossRef](#)]
36. Hanlon, T.; Kwon, Y.N.; Suresh, S. Grain size effects on the fatigue response of nanocrystalline metals. *Scr. Mater.* **2003**, *49*, 675–680. [[CrossRef](#)]
37. Ueno, H.; Kakihata, K.; Kaneko, Y.; Hashimoto, S.; Vinogradov, A. Enhanced fatigue properties of nanostructured austenitic SUS 316L stainless steel. *Acta Mater.* **2011**, *59*, 7060–7069. [[CrossRef](#)]
38. Li, Q.; Yan, F.K.; Tao, N.R. Enhanced fatigue damage resistance of nanotwinned austenitic grains in a nanotwinned stainless steel. *Scr. Mater.* **2017**, *136*, 59–63. [[CrossRef](#)]
39. Li, R.H.; Zhang, Z.J.; Zhang, P.; Zhang, Z.F. Improved fatigue properties of ultrafine-grained copper under cyclic torsion loading. *Acta Mater.* **2013**, *61*, 5857–5868. [[CrossRef](#)]
40. Rios, E.R.D.I.; Walley, A.; Milan, M.T.; Hammersley, G. Fatigue crack initiation and propagation on shot-peened surfaces in A316 stainless steel. *Int. J. Fatigue* **1995**, *17*, 493–499.
41. Dalaei, K.; Karlsson, B.; Svensson, L.E. Stability of shot peening induced residual stresses and their influence on fatigue lifetime. *Mater. Sci. Eng. A* **2011**, *528*, 1008–1015. [[CrossRef](#)]
42. Holzapfel, H.; Schulze, V.; Vöhringer, O.; Macherauch, E. Residual stress relaxation in an AISI 4140 steel due to quasistatic and cyclic loading at higher temperatures. *Mater. Sci. Eng. A* **1998**, *248*, 9–18. [[CrossRef](#)]